# A spectral-unmixing approach to estimate watermass concentrations in case 2 waters

# A spectral-unmixing approach to estimate water-mass concentrations in case-II waters

Dževdet Burazerović*, Rob Heylen*, Dries Raymaekers†, Els Knaeps†, Catharina J.M. Philippart ‡, Paul Scheunders*

* iMinds–Vision Lab, University of Antwerp, Wilrijk, Belgium

† Flemish Institute for Technological Research (VITO), Mol, Belgium

‡ Royal Netherlands Institute for Sea Research (NIOZ), Texel, The Netherlands

***Abstract*—In this work we study the estimation of water-quality parameters from the water-leaving reflectance by means of spectral unmixing. Our starting point is the provision of an analytic model relating the reflectance of water to its masses/bodies or constituents, as specified by their specific inherent optical properties (SIOP) and concentrations. The main objective is to reformulate the estimation of these concentrations as a spectral unmixing problem. We do this by employing the linear mixing model, while suitably taking the endmembers as representations of different water types dominated by one or more constituents. Each endmember is then calculated by substituting the in *situ* measured SIOP and combinations of utmost concentrations of each constituent into the water-reflectance model. Such use of unmixing practically enables to maintain an implicitly nonlinear relation between the water reflectance and constituents' concentrations, without resorting to the use of nonlinear mixing models. Furthermore, we present a method to automatically extract the endmembers from the reflectance image. We validate the entire unmixing-based take using as reference a state-of-the-art method that inverts the water reflectance via comparisons (curve matching) with spectra from a look-up table. This validation is done using simulated data derived from the water-reflectance model and real hyperspectral data acquired over coastal waters of a shallow sea.**

***Index Terms*—Remote sensing, image processing, water quality retrieval, spectral unmixing, case 2 waters**

## I. Introduction

Monitoring of water quality in inland and coastal waters is a vital study area within the all-important field of hydrological observation and water-resource management. Traditionally, the composition and dynamics of water have been gauged using in *situ* measurements that offer a point-based sampling of the water surface [1]. However, due to the cost and limitations of this methodology in providing extensive spatial and temporal coverage, the use of remote sensing has been proliferating in recent years. The different modalities and techniques are here considered mostly in conjunction with strategic in *situ* sampling, which then serves to derive model parameters or establish a ground-truth reference [1].

The basic idea upon which rest all water-quality retrieval algorithms is that the water-leaving reflectance (visible and near-infrared light leaving the water column) of a water surface is largely shaped by the identity and concentration of in-water substances or constituents. The exact definition of a water constituent can vary (see e.g. [2] and references therein), but in coastal and inland waters those that are optically active are: *colored dissolved organic matter* (CDOM), *total suspended matter* (TSM) and *chlorophyll-a* (CHL). Furthermore, most inland and coastal waters can be classified as 'case 2', which means that all these constituents vary independently from each other. These observations have inspired many studies in which the water-leaving reflectance is essentially inverted to obtain the unknown concentrations. This naturally assumes that all sources which, in addition to the water-leaving reflectance, contribute to the remote sensed signal should be modeled and removed. Examples of these influences are sun- or sky glint [3], atmospheric effects [4] or bottom reflectances.

One of the prerequisites for inverting the water-leaving reflectance in an analytical model is to express it in terms of the total absorption and backscatter, or the *inherent optical properties* - IOP, of each water constituent. There exist several models that do so via first-order rational functions [5] or more complex extensions thereof [6]. The second element is to write IOP as products of concentration-*specific* IOP, or SIOP, and the respective concentrations. When the SIOP are known (e.g. from in *situ* or lab measurements), this enables to estimate the concentrations directly from the observed reflectance. One common way of doing so has been to apply the ordinary least squares (OLS), i.e. linear regression [7]. Another approach has been to use training of artificial neural networks [8]. Yet another route is to invert the spectrum indirectly, by comparing it with a library constructed by substituting known (measured or extrapolated) concentrations into the water-reflectance model [9]. A worthwhile study from this category, albeit with a somewhat different focus – mapping of microphytobenthos biomass, is also found in [10]. In general, the main limitation of all model-based methodology is its sensitivity to variations in the reflectance signal, which can be due to sensor noise, variation of SIOP, or inadequate estimation and correction of the atmospheric effects.

Recently, a different take on the estimation of water-mass concentrations in coastal and inland waters was elaborated in [2] making use of spectral unmixing. In this paper, we reaffirm and extend this approach. The central idea is to employ the *linear mixing model* (LMM) [11], wherein the endmembers are defined as representations of different *water types* dominated by one or more constituents. Each endmember is then in effect calculated by substituting the known (in *situ* measured) SIOP and in turn utmost concentrations of each constituent into an adopted water-reflectance model.

Despite the demonstrated ability of this approach to yield good reconstruction of the water spectra, its only qualitative translation of the unmixing result to unknown concentrations and extensive reference to in *situ* measured data remain a limitation. We mitigate this by introducing several add-ons. To start with, we explore extractability of the endmembers from the data. With the extracted endmembers, we perform unmixing and derive a relation between the obtained abundance maps and water-mass concentrations, based on ground reference data. From this, actual concentration maps are obtained. We then compare these maps with those produced by a state-of-the-art, curve-matching method.

The sequel of this paper is organized as follows. In Sec. II, we describe the prevalent model for relating the reflectance of water to in-water constituents of interest that will serve as a basis for our analysis. Here, we shall also clarify the most common procedures for inverting this model. The core of our study, which is to link the water reflectance to spectral unmixing, is described in Sec. III. An important part here will be devoted to our proposal for automating the endmember extraction. In Section IV we discuss our experiments on simulated and real hyperspectral data, while Section V summarizes with general conclusions and discussion.

## II. Water reflectance modeling

A common way to analytically relate reflectance of water to its constituents (see e.g. [2], [12], [7]) is via the Gordon model [5], which is typically formulated as:

$$\hat{R}(0-,\lambda) = f \cdot \frac{b(\lambda)}{a(\lambda)+b(\lambda)} \tag{1}$$

where $R(0-)$ is the subsurface irradiance reflectance (depth = 0-) and we use the accent to distinguish the modeled reflectance from the observed (ship-based or airborne) one. Furthermore, $a$ and $b$ denote the total absorption and backscattering coefficients of all water constituents, and $f$ is a parameter that is specifically related to illumination and viewing conditions but is usually assumed constant for particular water surface (e.g. for typical Dutch inland waters it was found that $0.2 \leq f \leq 0.59$ [13]). While other models certainly exist, it is fair to say that most connote some variation of (1), obtained by using more elaborate definitions of $f$, or using $b/(a+b)$ as a factor in more complex formulas including e.g. higher-order polynomials ( [14], [6]). We leave aside these elaborations and concentrate on (1), where we shall hence omit $f$ and suppress the wavelength dependency to yield simplified notations. We shall bring this dependency up again wherever required by the context.

A typical assumption in the above analysis is that both $a$ and $b$ can be decomposed as linear sums of contributions from pure water (seawater) and the other mentioned in-water constituents: CDOM, TSM and CHL. The constituent terms can in turn be written as products of concentration-specific IOP ($a$ and $b$), or SIOP, and the corresponding concentrations, i.e. $a_{\mathtt{CHL}} = a^\star_{\mathtt{CHL}}\mathtt{CHL}$, $a_{\mathtt{CDOM}} = a^\star_{\mathtt{CDOM}}\mathtt{CDOM}$, etc. Another convention decomposes the IOP into water, dissolved and particulate fractions [15]. This dictates splitting the absorption of TSM into its particulate (phytoplankton or algae) and the Non-Algae-Particles (NAP) part [16], i.e., $a_{\mathtt{TSM}} = a_{ph} + a_{\mathtt{NAP}}$. As still the NAP are dominant in complex waters under consideration, the NAP and TSM concentrations can be assumed to be equal and we can write [17] $a_{\mathtt{NAP}} = a^\star_{\mathtt{NAP}}\mathtt{TSM}$. Due to negligible (back)scatter for dissolved matter [17], one derives the following expressions for the IOP:

$$\begin{aligned} a &= a_w + a^\star_{\mathtt{NAP}}\mathtt{TSM} + a^\star_{\mathtt{CHL}}\mathtt{CHL} + a^\star_{\mathtt{CDOM}}\mathtt{CDOM} \\ b &= b_w + b^\star_{\mathtt{NAP}}\mathtt{TSM} \end{aligned} \tag{2}$$

where $a_w$ and $b_w$ are the absorption and backscatter of pure water, $a^\star_i$, $b^\star_i$ are the SIOP, and $\mathtt{TSM}$ ($\mathrm{g/m^3}$), $\mathtt{CHL}$ ($\mathrm{mg/m^3}$) are concentrations. Furthermore, concentration of CDOM is defined by its absorption [16], [18]:

$$a_{\mathtt{CDOM}}(\lambda) = a^\star_{\mathtt{CDOM}}(\lambda_r)e^{-S(\lambda_r-\lambda)} \tag{3}$$

where $a^\star_{\mathtt{CDOM}}(\lambda_r)$ is the absorption $(m^{-1})$ at a reference wavelength. A similar exponential formula is also used for $a^\star_{\mathtt{NAP}}(\lambda)$, and since absorptions of NAP and CDOM are difficult to distinguish, ocean color algorithms generally retrieve their sum [15], [19]. Inserting $a$ and $b$ from above into (1), while omitting $f$, then yields:

$$\hat{R} = \frac{b_w + b^\star_{\mathtt{NAP}}\mathtt{TSM}}{a_w + b_w + (a^\star_{\mathtt{NAP}} + b^\star_{\mathtt{NAP}})\mathtt{TSM} + a^\star_{\mathtt{CHL}}\mathtt{CHL} + a^\star_{\mathtt{CDOM}}\mathtt{CDOM}} \tag{4}$$

or equivalently:

$$\begin{aligned} (a^\star_{\mathtt{NAP}} + b^\star_{\mathtt{NAP}}\tilde{R})\mathtt{TSM} + a^\star_{\mathtt{CHL}}\mathtt{CHL} + a^\star_{\mathtt{CDOM}}\mathtt{CDOM} = \\ -a_w - b_w\tilde{R}\,, \text{ where } \tilde{R} = (\hat{R}^{-1} - 1) \end{aligned} \tag{5}$$

These formulas permit to clarify some of the approaches for inverting $\hat{R}$ that we mentioned in Sec. I. Specifically, one way to estimate the unknown concentrations is by taking $\hat{R}$ and $a_i$, $b_i$ in (5) at $n \geq 3$ wavelengths, yielding a full-column-rank system $\boldsymbol{A}\boldsymbol{c} = \boldsymbol{y}$ that can be solved by OLS, i.e. $\hat{\boldsymbol{c}} = (\boldsymbol{A}^{\mathrm{T}}\boldsymbol{A})^{-1}\boldsymbol{A}^{\mathrm{T}}\boldsymbol{y}$, where $\boldsymbol{c} = (\mathtt{TSM}, \mathtt{CHL}, \mathtt{CDOM})$ is the vector of concentrations,

$$\boldsymbol{A} = \begin{bmatrix} a^\star_{\mathtt{NAP}}(\lambda_1) + b^\star_{\mathtt{NAP}}(\lambda_1)\tilde{R}(\lambda_1) & a^\star_{\mathtt{CHL}}(\lambda_1) & a^\star_{\mathtt{CDOM}}(\lambda_1) \\ \vdots & \vdots & \vdots \\ a^\star_{\mathtt{NAP}}(\lambda_n) + b^\star_{\mathtt{NAP}}(\lambda_n)\tilde{R}(\lambda_n) & a^\star_{\mathtt{CHL}}(\lambda_n) & a^\star_{\mathtt{CDOM}}(\lambda_n) \end{bmatrix}$$

and $\boldsymbol{y} = (-a_w(\lambda_1) - b_w(\lambda_1)\tilde{R}(\lambda_1), \ldots, -a_w(\lambda_n) - b_w(\lambda_n)\tilde{R}(\lambda_n))$. Notice that the inverse $(\boldsymbol{A}^{\mathrm{T}}\boldsymbol{A})^{-1}$ must be computed for each data point, due to the dependence of both $\boldsymbol{A}$ and $\boldsymbol{y}$ on the input reflectance, via $\tilde{R}$. In the literature, it has often been remarked that the said OLS solution will not guarantee all positive values in $\boldsymbol{c}$ [12]. This has sometimes been circumvented by fixing one of its components, e.g. $\mathtt{CDOM}$ [7], which also seems justified considering the aforementioned indistinguishably of $a^\star_{\mathtt{CDOM}}$ and $a^\star_{\mathtt{NAP}}$. We ought to add that non-negativity of $\boldsymbol{c}$ as a solution to $\boldsymbol{A}\boldsymbol{c} = \boldsymbol{y}$ should in principle also be attainable by applying the NNLS algorithm by Lawson and Hanson [20].

A popular alternative to this matrix inversion has been to avoid it altogether, by constructing a library of spectra, $\{\tilde{R}_i\}$, to be matched the observed spectrum, $\hat{R}$. The library spectra are then obtained by inserting known SIOP $(a^\star_i, b^\star_i)$ and concentrations ($c_i \in \{\mathtt{TSM}, \mathtt{CHL}, \mathtt{CDOM}\}$) into the reflectance model; particularly, the model from (4) allows reading out directly the $\{c_i\}$ that produced some $\hat{R}$. There exist many

approaches that use this basic spectral matching idea, and they differ mostly in how they assess the difference between $\tilde{R}_i$ and $\hat{R}$. A recent study from [12] does this by looking at both the classical *root-mean-squared error*, $\texttt{RMSE} = E[(\tilde{R}_i - \hat{R})^2]$ and a difference between specific wavelet features from the two spectra. Another approach from [21] uses *simulated annealing* to optimize the RMSE over all spectra. In the sequel, we shall use the term 'curve-matching' to refer to a combination of these two methods, which had been used to produce results that we take as reference in our experiments.

We should remark that different treatments of the ocean color data certainly exist, where the above described methods belong to the prevalent group of *semi-analytical* algorithms. This term basically tells that the bio-optical stages of the *radiative transfer equation* are expressed by empirical relationships [22].

## III. A Spectral unmixing approach

When aiming to reformulate the water-quality retrieval as an unmixing problem, two basic angles can be taken. One is to try to reformulate some water reflectance model, like (4), as a mixing equation. For fixed SIOP, this may connote seeking a *multi-univariate* decomposition [23] of $\hat{R}$ as:

$$\hat{R} = g(h_1(c_1), h_2(c_2), h_3(c_3)),\ c_i \in \{\texttt{CHL}, \texttt{TSM}, \texttt{CDOM}\} \quad (6)$$

where $g(\cdot)$ would ideally stage some mixing function, giving the univariates $\{h_i(c_i)\}$ the role of independent endmembers. By inverting the $g(\{h_i\})$, and in turn each of the $\{h_i(\cdot)\}$, one could then directly translate the endmember abundances to wanted concentrations: $\{c_i\}$. Unfortunately, a clear obstacle for decomposing (4) is its low polynomial order.

The alternative, then, is to adopt some known mixing model and contemplate a suitable definition of endmembers. As we will see, by combining the classical LMM with 'hybrid' endmembers defined from (4), a nonlinear relation between $\hat{R}$ and $\{c_i\}$ can be amply covered. Complexity of this relation will disallow exact, quantitative translation from the endmember abundances to concentrations $\{c_i\}$, but we will derive this by referring to the available ground-reference data.

Surely, one can argue that nonlinear (e.g. bilinear) unmixing models may be equally applied using a same or different definition of endmembers. Yet, based on the previous argument and results from [2], it is unsure if this would yield a worthwhile supplement (in terms of interpreting the unmixing result or lowering the reconstruction error) on top of the much simpler LMM-based approach. Another distinctive take on unmixing may consist of storing the signatures of water endmembers in a dictionary and applying (sparse) regression. A counterargument for such use is that it would resemble more the reference curve-matching methodology, whereby the water spectra are also compared with a library, only directly.

For the sake of completeness, we proceed by giving a brief explanation and reference to several methods of spectral unmixing. Our focus will then turn to an LMM-based approach, where we will offer an additional motivation, and present a method for extracting the endmembers from the data.

### A. Spectral unmixing

Spectral mixing refers to the situation when multiple intrinsic (e.g. ground cover) materials contribute to the spectrum that is observed for a single pixel. The unraveling of such mixed pixels has been widely addressed in the literature as *spectral unmixing*, which has been tackled using both linear and non-linear paradigms and models [11], [24], [25], [26]. One typical assumption of the prevalent linear mixing model (LMM) is that the incident photons will interact with each material once before reaching the sensor. This is viable when the mixing scale is macroscopic and no secondary reflections occur due to topography and multi-layering of reflective surfaces in the scene. The spectrum of the mixture can in this case be faithfully represented as a linear sum of the spectra of its constituents [11], which is put mathematically as:

$$\hat{\boldsymbol{x}} = \sum_{i=1}^{p} a_i \boldsymbol{e}_i + \boldsymbol{n}, \quad \forall i:\ a_i \geq 0\,,\ \sum_{i=1}^{p} a_i = 1 \quad (7)$$

where $\boldsymbol{x} = (r_1, \ldots, r_l)$ is the $l$-dim. spectrum of a pixel and $\boldsymbol{e}_i = (e_{i1}, \ldots, e_{il})$ are the spectra of intrinsic materials, the so-called *endmembers*, constituting the mixture. Furthermore, $p$ denotes the known or estimated number of endmembers, $a_i$ is the fractional representation or *abundance* of endmember $\boldsymbol{e}_i$ in pixel $\boldsymbol{x}$, while $\boldsymbol{n}$ stands for additive modeling errors and noise. Considering the system of equations (7) for $l \geq p$ makes it solvable with ordinary least-squares; however, a physically more meaningful solution is obtained by also imposing the indicated positivity- and sum-to-one constraints. This is simply saying that only the whole pixel area and no negative sub-pixel areas are taken into account. When the $\{\boldsymbol{e}_i\}$ in (7) are known, the inversion needed to determine the $\{a_i\}$ can be attained by applying the established fully constrained least-squares optimization (FCLSU) [27].

The search for endmembers $\{\boldsymbol{e}_i\}$ is then often treated as a separate problem. A widely used methodology is to exploit the geometry implied by (7) and saying that, for $\boldsymbol{n} = 0$, all $\{\boldsymbol{e}_i\}$ correspond to vertices of a $(p-1)$–simplex enclosing all the $\boldsymbol{x}$. Finding the $\{\boldsymbol{e}_i\}$ then becomes equivalent to finding or constructing those points in the data that will yield a simplex enclosing most of that data, while preferably excluding outliers and noise. Some of these concepts are also clarified in Fig. 1 showing a 3-simplex enclosing 2-dimensional data. For a point $\boldsymbol{x}$ inside the simplex, its abundance with respect to endmember $\boldsymbol{e}_i$ can be determined as [28]:

$$a_i = \frac{V_{\{1,\ldots p\}\setminus\{i\}}}{V} = \frac{V(\boldsymbol{e}_1, \ldots, \boldsymbol{e}_{i-1}, \boldsymbol{x}, \boldsymbol{e}_{i+1}, \ldots, \boldsymbol{e}_p)}{V(\boldsymbol{e}_1, \ldots, \boldsymbol{e}_p)} \quad (8)$$

where $V$ is the volume of the simplex defined by $\{\boldsymbol{e}_i\}(i = \overline{1,p})$ and $V_{\{1,\ldots p\}\setminus\{i\}}$ the volume of a sub-simplex gotten by replacing $\boldsymbol{e}_i$ with $\boldsymbol{x}$. For an outside point, the step of computing distances from the endmembers is effectively preceded by orthogonally projecting that point onto the simplex. Note that performing these steps is equivalent to applying the aforementioned FCLSU [29], [30].

Besides this geometrical framework, several approaches exist that use priors (e.g. statistical or spatial-contextual) or place extra constraints on the solution of (7) (see [24] and references

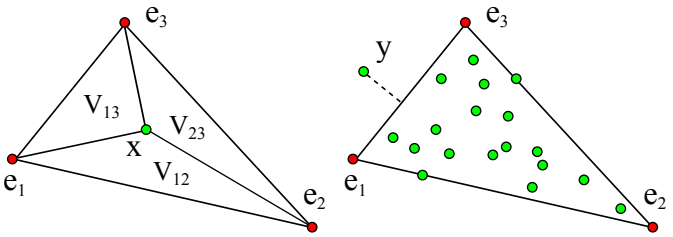


Fig. 1: Illustration of a 2–simplex and constructs for unmixing its interior- ($\boldsymbol{x}$) and an exterior point ($\boldsymbol{y}$).

therein). These constraints typically relate to the assumed sparsity, or rather plentifulness (a high degree of mixing) for the endmembers. Another distinctive approach expects some endmembers to be known beforehand (e.g. from lab measurements) and uses sparse regression [31], [32], thereby translating the problem to that of finding the optimal subset of endmembers in a spectral database.

### *B. Application of the LMM to water unmixing*

When contemplating spectral mixing with complex waters, one may intuitively think of intimate mixtures between pure water and other in-water constituents. One important difference with ground-cover mixing is that none of these constituents is expected to be observable as pure pixels, because none can exist in a 100% concentration in water solutions. This entails that water endmembers should anyhow designate compounds of pure water and multiple constituents, in varying concentrations. An implication is that the abundances of such endmembers will signify relative measures that can be more or less translatable to those (absolute) concentrations.

These observations were recently also exploited in [2], where the authors proposed to unmix water pixels using the fully-constrained LMM, while suitably defining the endmembers. Accordingly, each endmember was to represent a *water type* connoting a distinct but realistic mixture of the constituents. This was attained by inserting into (4) the SIOP and in turn extreme concentrations of each constituent, as extrapolated from in *situ* measurements. This unmixing can be expressed by (7), with the $\{\boldsymbol{e}_i\}$ specified by Table I. The table shows the possible combinations of lower- and upper limits for each concentration, i.e. $c_{i,\text{low}} = \min\{c_i(x,y)\}$ and $c_{i,\text{high}} = \max\{c_i(x,y)\}$, where $c_i \in \{\texttt{TSM}, \texttt{CHL}, \texttt{CDOM}\}$ and $(x,y)$ are the pixel coordinates. Notice that $c_{i,\text{low}}$ are chosen different from 0, as pixels with 100% concentrations are unfeasible in water solutions. The endmember $\boldsymbol{e}_1$ thus represents the spectrum of pure water, as characterized in e.g. [33].

One important thing to realize about this approach is that, although the adopted mixing model is linear, the reflectance $\hat{R}$ will relate nonlinearly to $\{c_i\}$ that determine its shape due to the definition of endmembers. Since several $\{\boldsymbol{e}_i\}$ from Table I use high concentrations for multiple constituents, writing out (7) with $\boldsymbol{x} = \hat{\boldsymbol{R}}$ while referring to Table I and Eq. (4) will yield an expression featuring non-negligible cross products of powers of $\{c_i\}$. This means that any shape of $\hat{\boldsymbol{R}}$ is likely to be well approximated by taking the $\{\boldsymbol{e}_i\}, (i = \overline{1,9})$ in various proportions, which are then easily computed by the FCLSU.

TABLE I: Combinations of $c_{i,\text{low}}$ and $c_{i,\text{high}}$, as in [2], yielding the endmembers (EM) when inserted into (4) with given SIOP.

| EM | TSM $(\text{g}/\text{m}^3)$ | CHL $(\text{mg}/\text{m}^3)$ | $a_{\text{CDOM}}$ $(440nm)$ $(1/m)$ |
|---|---|---|---|
| $\boldsymbol{e}_1$ | 0 | 0 | 0 |
| $\boldsymbol{e}_2$ | 1 | 1 | 0.2 |
| $\boldsymbol{e}_3$ | 1 | 1 | 3 |
| $\boldsymbol{e}_4$ | 1 | 60 | 0.2 |
| $\boldsymbol{e}_5$ | 1 | 60 | 3 |
| $\boldsymbol{e}_6$ | 100 | 1 | 0.2 |
| $\boldsymbol{e}_7$ | 100 | 1 | 3 |
| $\boldsymbol{e}_8$ | 100 | 60 | 0.2 |
| $\boldsymbol{e}_9$ | 100 | 60 | 3 |

**Algorithm 1** Estimate concentrations $c_i \in \{\texttt{TSM}, \texttt{CHL}, \texttt{CDOM}\}$

**Require:** $\{\hat{\boldsymbol{R}}_n\}_{n=1,\dots N}$ – water refl. image, $\{c_{i,m}\}_{m=1,\dots M}$ – in *situ* concentr. at $M$ pixels, $\{\boldsymbol{a}_w, \boldsymbol{b}_w, \boldsymbol{a}_i^\star, \boldsymbol{b}_i^\star\}$ – (S)IOP, $\{c_{i,\text{low}}, c_{i,\text{high}}\}$ – extremes of $\{c_{i,n}\}_{n=1,\dots N}$

1: Construct a dataset $\{\boldsymbol{R}_j\}$: Sample $c_i \sim U(c_{i,\text{low}}, c_{i,\text{high}})$ and insert these $\{c_i\}$ in Eq. (4).
2: Compute feature vectors: $\boldsymbol{R}_j \mapsto \boldsymbol{f}_j$ using Eq. (6)–(8).
3: Cluster $\{\boldsymbol{f}_j\}$ and save the cluster centroids $\{\boldsymbol{\mu}_k\}_{k=1,\dots K}$
4: $\hat{\boldsymbol{R}}_n \mapsto \boldsymbol{f}_n$ and assign the pixel spectra to clusters: $\hat{\boldsymbol{R}}_n \mapsto C_k\,, k = \arg\min(\|\boldsymbol{f}_n - \boldsymbol{\mu}_k\|)$
5: Extract endmembers $\{\boldsymbol{e}_{k,l}\}$ from $\{C_k\}$.
6: Compute abundances $\{a_l\}$ by FCLSU inverting the LMM: $\hat{\boldsymbol{R}} = \sum_{l=1}^{p} a_l \boldsymbol{e}_l,\ a_l \geq 0\,, \sum_{l=1}^{p} a_l = 1$
7: Compute concentr. maps: $\boldsymbol{c}_i = \beta_{i,0} + \sum_{r\in S_i} \beta_{i,r}\, \boldsymbol{a}_r + \sum_{\substack{r,q\in S_i \\ r\neq q}} \beta_{1,rq}\, \boldsymbol{a}_r\, \boldsymbol{a}_q$. Derive $\beta_{i,(.)}$ by regressing on $\{c_{i,m}\}$.
8: **return** $\{c_{i,n}\}_{i=1,\dots 3; n=1,\dots N}$

Looking at the described endmember model, we see that it can yield relatively interpretable but realistic unmixing, as all $\{\boldsymbol{e}_i\}$ are defined by fully exploiting the data acquired from in-*situ* measurements. One objection to such use is that it also reduces the distinctiveness of unmixing relative to other inversion methods (see Sec. II) that use such data. Hence, one of our goals next is to investigate if the $\{\boldsymbol{e}_i\}(i = \overline{1,9})$ from Table I can also be extracted from the data itself. It is clear that reference to (4) and Table I is unavoidable, if one is to identify the extracted $\{\boldsymbol{e}_i\}$. So we could also take knowledge this upfront into the extraction process. Nevertheless, posterior matching of the $\{\boldsymbol{e}_i\}(i = \overline{1,9})$ to a small subset of candidates extracted in a data-driven way can be a convenient way of dealing with homogeneity of water spectra, especially when collected from large water content.

Algorithm 1 gives an overview of several steps we discuss in the sequel. To examine the extractability of the $\{\boldsymbol{e}_i\}(i = \overline{1,9})$, we first construct a test data using our knowledge of (4) and Table I. Based on analysis of this data, we design a specific endmember-extraction (EE) strategy combining common data clustering and EE techniques. The clustering will use not the full spectra, but features (shape descriptors) we derive from those. We then use the extracted $\{\boldsymbol{e}_i\}$ to unmix a real image via the FCLSU, to obtain the abundances $\{a_i\}$. Finally,

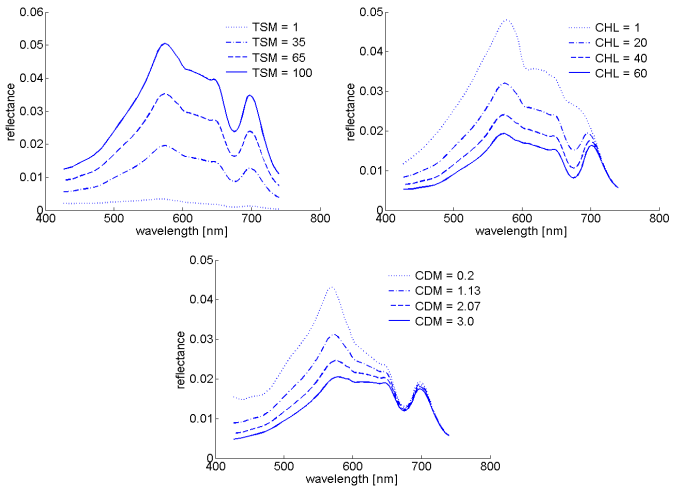


Fig. 2: The effect of varying $c_i \in [\texttt{TSM}, \texttt{CHL}, \texttt{CDOM}]$ within its range while keeping $c_j, j \neq i$ constant (at their range average.)

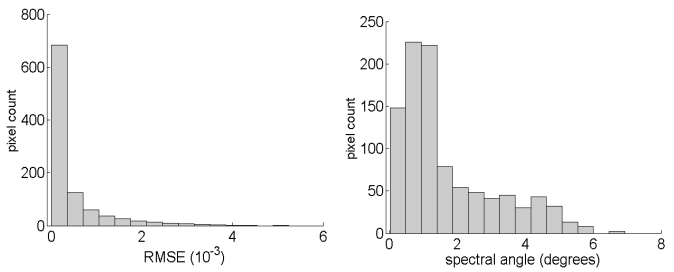


Fig. 3: Reconstruction error for the endmember model on 1000 samples of the constructed (simulated) data.

we use available ground-truth pixels to derive a model that will translate these $\{a_i\}$ to full concentration maps. The last mentioned step will be described in Sec. IV.

We ought to point out that all further discussion will assume that the SIOP are known. These SIOP will in effect comprise data from our in *situ* measurements, as detailed in Sec. IV.

### C. Assesment of the endmember model

The first question to ask is whether the $\{\boldsymbol{e}_i\}, (i = \overline{1,9})$ from Table I do in fact represent true (geometric) endmembers. A direct way to ascertain these $\{\boldsymbol{e}_i\}$ as the extremes of $\hat{R}$ from (4) is to study this as a trivariate function of $\{\texttt{TSM}, \texttt{CHL}, \texttt{CDOM}\}$. Yet, the fact that $\hat{R}$ is at the same time a function of the SIOP, which themselves depend on $\lambda$, makes this impractical. Still, by varying each $c_i$ while fixing the others, we learn that different ranges of $\{c_i\}$ affect mostly distinct parts of $\hat{R}$, which in turn means that discerning not only its shape but also the scale is relevant. Figure 2 gives an illustration. Notice that the visible wavelengths are the most discerning, as all water spectra tend to converge in the near-infrared (NIR) range [34].

Another and more empirical way to ascertain the $\{\boldsymbol{e}_i\}$ is to affirm them as being the vertices of a minimum-volume enclosing simplex. This is even more interesting since knowing (4) allows us to construct a perfectly representative test data. If (4) describes any water spectrum, and the SIOP and $\{c_{i,\text{low}}, c_{i,\text{high}}\}$ from Table I are known, then all possible spectra can be obtained by inserting into (4) random, uniformly distributed $c_i$, i.e. $c_i \sim U(c_{i,\text{low}}, c_{i,\text{high}})$. With the known SIOP and $c_{i,\text{low}}$, $c_{i,\text{high}}$ from Table I, we use this notion to construct several sets counting from $10^3$ to $20^3$ samples, which practically connotes varying each $c_i$ with steps between $5 - 10$ %. Moreover, we account for perturbation in some SIOP ($a^\star_{\texttt{CHL}}$, $a^\star_{\texttt{TSM}}$, $b^\star_{\texttt{TSM}}$) by shifting each randomly within its error range, equaling the standard deviation ($\sigma$) from the mentioned in *situ* measurements. Here, the *signal-to-noise ratio* for the different SIOP (averaged over all wavelengths and computed as $SNR = 20\log_{10}(\mu/\sigma)$, with $\mu$ being the signal average) lied between 10dB and 16dB.

To affirm the $\{\boldsymbol{e}_i\}$ as endmembers in this test data, we regard several options. One is to examine the inwardness of the data relative to the simplex defined by the $\{\boldsymbol{e}_i\}$. This is done by computing (8) and checking the additivity $\sum_j a_{k,j} = 1$, after first projecting all $k$ points onto the simplex plane, i.e. a subspace of dimensionality $p - 1$ containing the endmembers. Another possibility is to simply see which of the $\{\boldsymbol{e}_i\}$ can be identified by EE algorithms [24]. We conclude that most $\{\boldsymbol{e}_i\}$ were rightfully designated as endmembers, where $\{\boldsymbol{e}_3, \boldsymbol{e}_4, \boldsymbol{e}_5\}$ gave inconsistent results.

Finally, we unmix the test data by employing the FCLSU and $\{\boldsymbol{e}_i\}$ from Table I to assert the coverage of the endmember model. We compute two error measures – *root-mean-square error* (RMSE) and *spectral angle* [11] between the original and reconstructed spectra, $\{a_i\boldsymbol{e}_i\}$. Figure 3 shows this result. We conclude that the majority of possible combinations of $c_i \in \{\texttt{TSM}, \texttt{CHL}, \texttt{CDOM}\}$ in (4)) is well reconstructed, with few apparently being 'out of reach' of the endmember model. This may in part be attributed to the use of unmixing constraints.

### D. Feature extraction and clustering

Unlike with the simulated data, an indiscriminate use of unsupervised EE algorithms may yield poor detection of $\{\boldsymbol{e}_i\}$ in real (and large) water content, due to greater homogeneity of those spectra. We will alleviate this problem by reducing the search space for the EE algorithms. Inspired by our analysis of the constructed dataset from the previous section, we reckon that all water spectra exhibit limited shape variation that can be accommodated by grouping them into several clusters. One effect we expect from clustering is that it can set apart some $\{\boldsymbol{e}_i\}$ by making them appear at the boundaries of clusters.

Clustering of water spectra has been explored before for both classification and to define endmembers – as being the cluster centroids, where the input to this clustering have typically been the full spectra in their original, differentiated or normalized form (see [2] and references therein). Similar use of clustering has been reported outside the water-retrieval context [35], [36]. However, to us the main goal of clustering is different, namely to reduce the search space prior to EE.

We consider common clustering methods, such as *k-means* and others [37]. Instead of using the entire spectra, we will describe their shapes by extracting some fast-computable, and even more importantly, scale-invariant features. This shape invariance means that the features should reflect a spectral

shape faithfully even if the spectra are offset, e.g. due to miscalculation of factor $f$ from Eq. (1).

The first set of features we consider are *Fourier Descriptors*:

$$r[k] = \sum_{n=1}^{N} \hat{R}[n] e^{\frac{-i2\pi}{N}(k-1)(n-1)}, (k = 1 \ldots, N) \quad (9)$$

where $\hat{R}[n] \equiv \hat{R}(\lambda_n)$ is a water spectrum and $N$ is the number of wavelengths. The formula basically describes the discrete Fourier transform generating a signal $r$ of the same length as the input signal $\hat{R}$. However, for meaningful and robust shape discernment, and to be independent on the signal level, we take as features only the absolute values of few initial coefficients normalized by the first coefficient:

$$f_i = |r[i+1]/r[1]| \ , \ i = 1, 2, 3 \quad (10)$$

Another variable we consider is the *unsigned curvature*:

$$\kappa[n] = \frac{|\ddot{\hat{R}}|}{(1 + \dot{\hat{R}}^2)^{3/2}} \ , \ f_4 = \frac{1}{N-1} \sum_{n=1}^{N} (\kappa[n] - \overline{\kappa})^2 \quad (11)$$

of which we take as feature its *standard deviation* as shown. The symbols $\dot{\hat{R}}$ and $\ddot{\hat{R}}$ stand for the first- and second derivative of $\hat{R}$, and $\overline{\kappa}$ is thus the average of $\kappa[n]$. This way, we produce a total of 4 features, which we take in their normalized form: $\|f_i\| = f_i / \max(f_i)$ to give each feature an equal weight.

We ought to remark that this choice of features is certainly not exclusive, as other signal transforms, like e.g. *wavelets*, have been demonstrated to be useful in quantifying the shapes of water spectra [38]. However, where these transforms can be effective in capturing local signal variations [12], our $\{f_i\}, (i = \overline{1,4})$ are adequate for discerning the entire spectra.

To test these features and clustering, we compute them with the simulated dataset from Sec. III-C. We then validate the clustering using some common measures. One is the *silhouette index*, which measures heterogeneity and isolation of clusters by averaging a confidence measure on the membership of each sample in particular cluster. Another is *Davies-Bouldin (DB) index* that identifies sets of compact and well-separated clusters by measuring intra- and inter-cluster distances. The exact mathematical formulation is found in e.g. [39]. We compute these measures on the basis of multiple runs, with each run using a same clustering algorithm (*k-means*) but a different number of clusters. Figure 4 shows a typical result obtained when using all 4 features. We see that the iteration with 4 clusters produced a clear optimum: low *DB*- and high *silhouette* index [39]. This tells us that the features are indeed capable of producing well-separated clusters.

This performance is further illustrated in Fig. 5, which shows randomly chosen spectra from each cluster, along with some of the $\{e_i\}$ from Table I. Indexed as in a $3 \times 2$ matrix, the clusters are interpreted as follows. The top two rows show the 4 clusters ('11', '12', '21' and '22') obtained when using the $\{f_i\}, (i = \overline{1,4})$ from (9)-(11). The bottom row shows another layer of clustering, i.e. two extra clusters obtained by subdividing two of the initial 4 clusters based on single features: $f_1$ and $f_5 = f_1/f_2$. In particular, the sub-cluster '31' (bottom left) is derived from the cluster '11' and the sub-cluster '32'

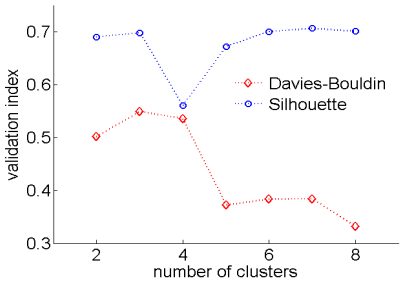


Fig. 4: Cluster validation with simulated spectra.

from the cluster '21'. Notice that several $\{e_i\}$ are identifiable at the boundaries of these clusters, as we had also anticipated.

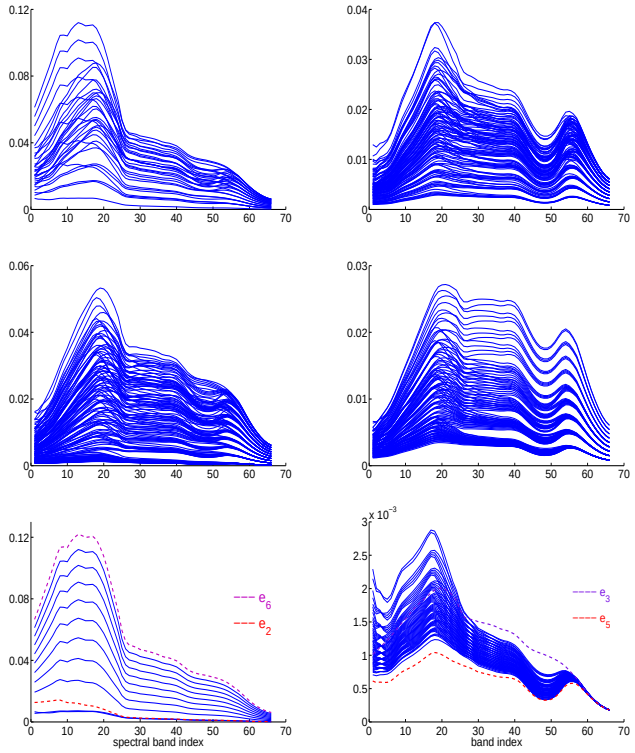


Fig. 5: A result of clustering of 1000 simulated spectra with the proposed features. The bottom row shows two sub-clusters and the matching endmembers from Table I.

It is now clear that the result of this clustering – the cluster centroids (and the feature scaling factors $\{f_{i,\max}\}$) could be reused with other data, if that data will originate from water content with SIOP and $\{c_{i,\text{low}}, c_{i,\text{high}}\}$ in the similar ranges. The benefit of such use is that each new pixel gets assigned to a cluster by comparison with few readily available points (the centroids), leading to fast, sequential processing.

### *E. Endmember extraction*

For the actual endmember extraction, two strategies can be followed. Either we perform EE on each of the found clusters separately (cluster-based approach), or alternatively we apply EE on the entire image, without using the clustering (image-based approach). Doing both at the same time will give us an

extended set of candidate endmembers that we can coalesce and sort using additional criteria. One of those criteria can be the ability of a subset of candidates to maximize the sum of their pairwise distances, as an indication of the largest simplex. Another can be the proximity of each candidate to one of the cluster centroids, or to a feature-vector representation of the predefined $\{\boldsymbol{e}_i\}, (i = \overline{1,9})$ from Table I.

In our analysis of the simulated data in Sec. III-C, we saw that the geometrical EE methods that search for extremes in the data were successful in detecting most of the $\{\boldsymbol{e}_i\}, (i = \overline{1,9})$. We also know that these $\{\boldsymbol{e}_i\}$ were defined using the same Gordon model that is used to represent any other pixel. Therefore, for the EE step, we adopt some prevalent geometrical algorithms, such as N-findR [40] and VCA [41]. Their imperfection in detecting some of the $\{\boldsymbol{e}_i\}$ in real data should then be compensated by the clustering step.

## IV. Unmixing experiments

This section describes our experiments with real hyperspectral data. To keep our objectives straight, we structure these experiments in two parts. After describing the image, we first discuss unmixing of that image with the predetermined endmembers from Table I. This will include the step of translating the abundances to actual concentration maps and comparing those with a reference obtained from curve matching. In the second part, we test the ability of our combined approach to extract matching endmembers from the image itself and to produce similar result.

### A. Description of the hyperspectral data

We consider an APEX image acquired over the Wadden Sea area in the Netherlands, in June, 2011. APEX is developed by a SwissBelgian consortium on behalf of ESA and is intended as a simulation, calibration and validation device for spaceborne imagers. The APEX sensors record data in about 300 bands covering the range of 380-2500 nm [42]. The radiometric, spectral and geometric calibration is performed by the Calibration Home Base (CHB) hosted at DLR Oberpfaffenhofen, Germany [43]. The atmospheric and air-interface correction of the acquired data was done with the MODTRAN-4 radiative transfer code following the algorithms and their implementation described in [44], [45]. Residual sky glint was corrected by subtracting the reflectance remaining at 1203 nm.

The Wadden Sea area is regarded as suitable for studying water composition, because it includes coastal and shallow waters that are known to be subject to land, oceanic and human influences [2]. The Marsdiep, the westermost tidal inlet of the Wadden Sea, is particularly suited for our purpose, because it contains different water types at short distance. Here marine waters from the open sea in the west mix with freshwater originating from a channel in the south and a highly productive freshwater lake in the east. Figure 6 shows an extended view of the scene, where it is seen that the image is registered as a mosaic of multiple flight lines. Next to this image is a zoomed-in picture of a region of interest (ROI) that we select for unmixing. The selection was made mostly to get a more workable image size while including all the pixels bearing the

Fig. 6: RGB view of the test data: an extended view of the scene (*left*) and the zoomed-in ROI used for unmixing (*right*).

results from in *situ* measurements. Another concern was to include both the deep main channel as well as the shallow waters near the coast, as a way to increase the chance of finding most of the $\{\boldsymbol{e}_i\}$, i.e. pixels with concentration values approaching those from Table I. The spatial size of the ROI amounts around $1000 \times 1000$ pixels, with the pixel size 5.4m, and the spectral information has been confined to 65 bands in the 410-750nm range. Notice that the ROI includes surfaces other than water, which we used as an extra reference for masking out non-water-like pixels.

The SIOP and concentrations were measured for the 3 constituents: TSM, CHL and CDOM from water samples collected at the pontoon of NIOZ. From the water samples, TSM concentration was determined by filtering the water on Whatman GF/F glass fiber filters according to the European reference method $EN872(2005)$. Pigment analysis, including CHL-a concentrations were determined via HPLC. The concentrations at these locations resided in the following ranges: $\texttt{TSM}\,(\text{gm}^{-3}) \in [5.3, 10.2]$, $\texttt{CHL}\,(\text{mgm}^{-3}) \in [5.1, 10.4]$. The specific absorption spectra of non-algae particles and Chlorophyll were measured using the filter pad method using a LICOR integrating sphere attached to an ASD spectrometer following the methods described by [46] and REVAMP (Regional validation of MERIS chlorophyll products in North Sea coastal waters) protocols [47]. For the CDOM absorption, the water samples from the field campaign were temporarily stored in a cooled chamber and filtered through $0.2\mu$m pore size filters. To retrieve the CDOM absorption coefficient of the water samples, the beam attenuation of the filtered water was measured with Ocean Optics equipment in a transparent cuvet. As the data from the ocean optics equipment are noisy for wavelengths $< 400nm$ and $> 950nm$ the exponential shape of the CDOM absorption was fitted based on the $420 - 750nm$ wavelength range. More details about the concentration and SIOP measurement can be found in [48].

Overall, there was a satisfactory resemblance between the in *situ* measured spectra and those read from the corresponding pixels in the APEX image. The mean and standard deviation ($\mu_x \pm \sigma_x^2$) of two error measures – RMSE and *spectral angle* [11] computed between these spectra for 10 reference pixels were, respectively, $0.0059 \pm 0.0028$ and $10.7 \pm 2.7$ degrees. The same comparison between the in *situ* spectra and those obtained by inserting the in *situ* measured concentrations and

SIOP into (4) were $0.0054 \pm 0.0034$ and $10.5 \pm 3.8$. We should say that few relative outliers were responsible for most of the deviation. The factor $f$ required by (1) was also used and estimated at $f = 0.55$.

### *B. Unmixing with the predefined endmembers*

We start by unmixing the ROI image using FCLSU with all the $\{\boldsymbol{e}_i\}, (i = \overline{1,9})$ from Table I. This yields abundances $\{a_{ki}\}$ for each pixel $k$. First, we test the adopted unmixing model to represent the water spectra, which is verified by a low reconstruction error, as shown in Fig. 7 on the left.

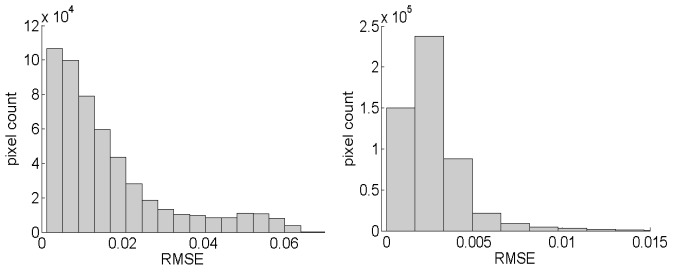


Fig. 7: Reconstruction error for the water spectra in the ROI image using the $\{\boldsymbol{e}_i\}, (i = \overline{1,9})$ from Table I (*left*) and for the extracted $\{\boldsymbol{e}_i\}$ from Fig. 11 (*right*).

Our main goal is to derive concentration maps for the constituents. However, translating the obtained abundances to concentrations is far from trivial. (Again, this is seen by writing out $\hat{x}$ from (7) as a sum of the fully expressed $\{\boldsymbol{e}_i\}\,(i = \overline{1,9})$ and equating this to $\hat{R}$ from (4).) Since we are most interested in CHL and TSM, we opt to derive their concentration maps while leaving CDOM out of the analysis.

In [2], a qualitative approach puts side-by-side the $\{a_{ki}\}$ and some $\{\hat{c}_{kj}\}$ representing the in *situ* measured values from a number of pixels. We propose a more quantitative approach and use the in *situ* measured values from our ground-truth pixels to derive a rule that will translate the $\{a_{ki}\}$ to concentrations $\hat{c}_j$, then extrapolate this to the entire image. We make use of an intuitive reasoning that $\hat{c}_j$ should relate to $\{a_i\}$ from those $\{\boldsymbol{e}_i\}$ that include $c_{j,\text{high}}$ in their definition. This means that we may write: $\texttt{TSM} \sim f(a_j)\,, j \in \{6,7,8,9\}$, $\texttt{CHL} \sim g(a_k)\,, k \in \{4,5,8,9\}$, etc., where $f$ and $g$ are some functions. Figure 8 shows the six abundances. The exact form of these functions is unknown, but since we are not using all $\{a_i\}\,(i = \overline{1,9})$, we can reasonably demand it to connote more than just a linear combination. Hence, for $c_1 \equiv \texttt{TSM}$ we consider *regression* with the interaction terms:

$$\boldsymbol{c}_1 = \beta_{1,0} + \sum_{k \in \{6,7,8,9\}} \beta_{1,k}\, \boldsymbol{a}_k + \sum_{\substack{k,l \in \{6,7,8,9\} \\ k \neq l}} \beta_{1,kl}\, \boldsymbol{a}_k\, \boldsymbol{a}_l \quad (12)$$

where $\boldsymbol{c}_1 = (c_{11}, \ldots c_{1n})$ has the in *situ* measured $c_1$ from $n$ ground-truth pixels, $\{\boldsymbol{a}_i\}$ are the $n \times 1$ vectors of abundances $a_i$ from each of those pixels, and $\beta_{1,\{.\}}$ are to be determined *regression coefficients*. The same is used for $c_2 \equiv \texttt{CHL}$ after replacing $a_6$ with $a_4$ and $a_7$ with $a_5$. Since in our case $n = 10$,

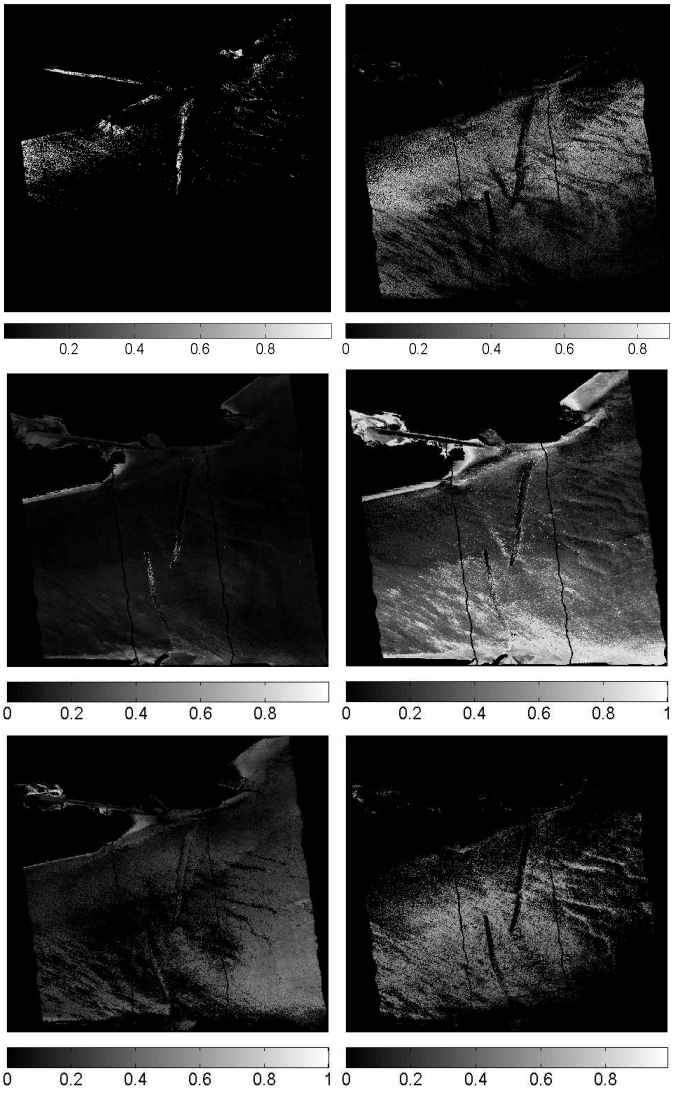


Fig. 8: From left to right and top to bottom: $\{a_4\}$, $\{a_5\}$, $\{a_6\}$, $\{a_7\}$, $\{a_8\}$ and $\{a_9\}$ produced by unmixing according to (7) with the $\{\boldsymbol{e}_i\}$ from Table I.

this method is prone to over-fitting. After some trials we retain these reduced models:

$$\begin{aligned} \boldsymbol{\beta}_1 &= (\beta_{1,0}, \beta_{1,6}, \beta_{1,7}, \beta_{1,8}, \beta_{1,\{6,7\}}, \beta_{1,\{6,8\}}) \\ \boldsymbol{\beta}_2 &= (\beta_{2,0}, \beta_{2,5}, \beta_{2,8}, \beta_{2,\{5,8\}}, \beta_{2,\{5,9\}}) \end{aligned} \quad (13)$$

where in the case of TSM we got a high *coefficient of determination*, $R^2 = 0.85$. This was notably lower with CHL ($R^2 = 0.6$), which can be ascribed to the fact that in all the ground-truth pixels there was a limited contribution from $a_5$ and none from $a_4$.

Figures 9 – 10 show the obtained concentration maps. As a comparison, maps produced by the curve-matching method are shown as well. It is worthwhile pointing out that the number of ground-truth pixels can be artificially increased, by taking the values of the curve-matching method from their neighborhood and assuming those to be equal to the in-situ measured values. When doing so, similar maps were obtained.

While it is clear why we had to be conservative with this ground-truth extension, the fact is that exaggerating it could provide an extra support for our argument about the coverage by the endmember model. We saw that by *linearly* combining the $\{\boldsymbol{e}_i\}\,(i=\overline{1,9})$ we could reconstruct most water spectra; now, we would see that with a properly derived (still simple, bilinear) combination of the abundances we could well reconstruct the concentration values themselves.

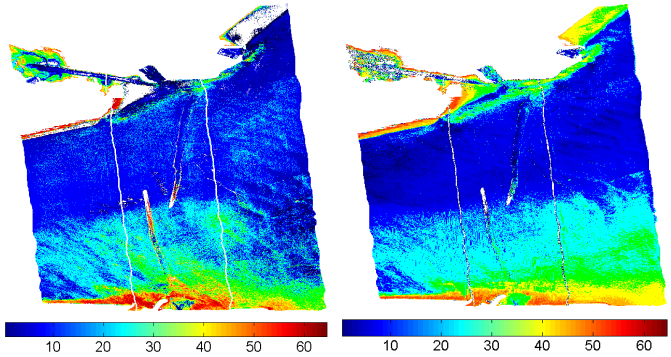


Fig. 9: Concentrations TSM ($\mathrm{g/m^3}$) obtained from $\{a_i\}$ subject to a model extrapolated from the ground-truth pixels (*left*), and from the curve-matching method (*right*).

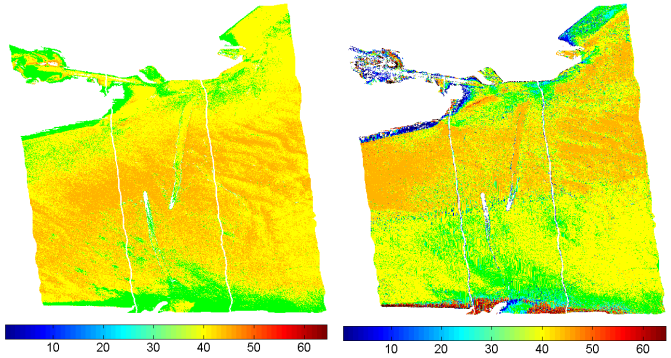


Fig. 10: The same comparison as in Fig. 9 for CHL ($\mathrm{mg/m^3}$).

### C. Endmember extraction and unmixing

The goal of the proposed clustering was to make a distinction between different spectral shapes that possibly relate to the target endmembers. We extract the $\{\boldsymbol{e}_i\}\,(i=\overline{1,9})$ following the same procedure as explained in Sec. III-E. Instead of clustering the real dataset, we re-use the cluster centroids obtained from clustering the simulated dataset.

After computing the features, the assignment of pixels to centroids did not produce the anticipated 4 clusters; in fact, only 3 properly filled clusters were obtained. This indicates that the spectra constituting our image did not exhibit all possible variety that we could theoretically expect based on our analysis of the simulated spectra. However, the second level of clustering did prove useful in spotting $\boldsymbol{e}_6$ and $\boldsymbol{e}_3$ at the sub-cluster boundaries, as explained in Sec. III-D.

For the EE-step, two strategies from Sec. III-E are followed: cluster-based EE and an image-level search in which no clustering is applied prior the EE-step. At the image level, we settled with searching for 7-8 endmembers. Per cluster, we set the target number of endmembers between 2 and 4. Thus, in total we generated up to 19 endmember candidates, which we sorted as explained in Sec. III-E. The final result is shown in Fig. 11. $\boldsymbol{e}_2$ is merely shown and not used in the analysis

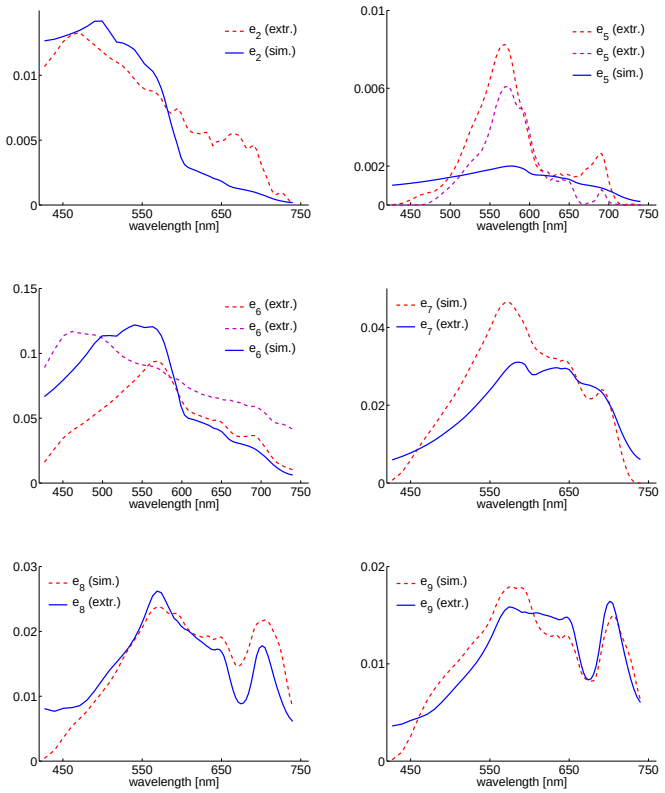


Fig. 11: Results of EE. The full lines depict $\{e_i\}$ from Table I and the dashed lines the matching spectra extracted from the image. For $e_5$ and $e_6$, the dotted lines show the results from the image-level search.

afterwards. Remark that $\boldsymbol{e}_4$ was not found using this analysis, which will influence the obtained concentration map of CHL. While the plots show mostly the results of the combined, cluster-based and global search, good approximations for $\boldsymbol{e}_2$, $\boldsymbol{e}_8$ and $\boldsymbol{e}_9$ were obtained from the global search alone. This was not true for $\boldsymbol{e}_7$ whose match was found thanks to the use of clustering. The best matches for $\boldsymbol{e}_5$ and $\boldsymbol{e}_6$ were obtained by averaging the results from the image- and cluster-based search. While one could argue that the extracted $\boldsymbol{e}_5$ deviates intolerably from the simulated one, assigning it was necessary to derive a decent map for CHL using the corresponding variant of (12).

Finally, we derive the concentrations from these extracted $\{\boldsymbol{e}_i\}$. The same procedure is followed as in the case of the simulated endmembers. Slightly different reduced models were used in the linear regression analysis. We will compare these with the concentrations obtained from the simulated $\{\boldsymbol{e}_i\}(i=\overline{1,9})$. We start by comparing the reconstruction errors using FCLSU obtained with the two sets of $\{\boldsymbol{e}_i\}$, which is shown in Fig. 7. We can see that the RMSE of the extracted $\boldsymbol{e}_i$ is lower.

This is explained by the relative homogeneity of the spectral shapes in our data that was already evident after the clustering step. The resulting concentration maps as shown in Fig. 12. Observe that the maps are somewhat different from those in Fig. 9–10 but the global trends remain largely similar. Because of the lack of $e_4$ in this analysis, the obtained concentration map of HCL deviates more from the curve-matching result.

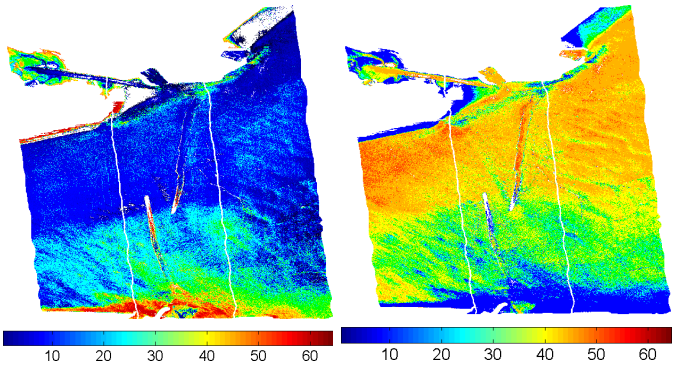


Fig. 12: Concentrations TSM (*left*) and CHL (*right*) obtained from the extracted $e_i$ from Fig. 11 and $\{a_i\}$ subject to a model derived from the ground-truth pixels.

## V. Conclusions, discussion and future work

We have described a method for studying the water quality by means of spectral unmixing. One of the main goals of our investigation has been to reaffirm unmixing as a viable method of estimating the water composition when the endmembers, specifying different water types, are known. To this end, we have designed and performed an extensive analysis of simulated spectra and conducted a comparison on real hyperspectral image using as reference a state-of-the-art, curve-matching method. To further advance the unmixing take, we have proposed methods to extract the endmembers from the reflectance data, as well as translate the endmember abundances to actual water-constituents' concentrations. The viability of this route has been confirmed by an acceptable resemblance between the unmixing-based results and the reference, and by an impacting similarity between the extracted and pre-specified endmembers.

The method for endmember extraction (EE) exploits a feature-based representation of the water spectra in combination with clustering and common EE techniques. Several of these components have been designed to explicitly use knowledge of the water-reflectance model and values of its parameters, such as the extreme concentrations of water constituents and their SIOP, while permitting some perturbation in those. This means that their extensibility for use with other water content will depend on whether the said parameters of that content will have similar values. The regression model for translating the abundances to concentrations has been derived from a limited ground truth, though, its build up is also more generally valid.

One of the important finding of our study is that linear unmixing with compounded endmembers defined from the water-reflectance model can amply cover variability of the water spectra. Nevertheless, in our future work we may seek extra gain from alternative endmember definitions and (nonlinear) unmixing equations.

## Acknowledgments

We are indebted to the Flemish Institute for Technological Research (VITO) for acquisition and preprocessing of the dataset. This work was partly funded by the project CHAMELEON of the Flemish Agency for Innovation by Science and Technology (IWT), and by the project IN PLACE of the Netherlands Organization for Scientific Research (NWO).

## References

[1] Z. Su, R. Roebeling, J. Schulz, I. Hollemann, V. Levizzani, J. Timmermans, H. Rott, N. Mognard-Campbell, R. De Jeu, W. Wagner, M. Rodell, M. S. Salama, G. Parodi, and L. Wang, "Observation of hydrological processes using remote sensing," in *Treatise on Water Science*, pp. 351–399. Elsevier, Oxford: Academic Press, 2011, invited.

[2] A. Hommersom, M.R. Wernand, S. Peters, M. A. Eleveld, H. J. van der Woerd, and J. de Boer, "Spectra of a shallow sea - unmixing for class identification and monitoring of coastal waters," *Ocean Dynamics*, pp. 463–480, 2011.

[3] S. Kay, J. D. Hedley, and S. Lavender, "Sun glint correction of high and low spatial resolution images of aquatic scenes: a review of methods for visible and near-infrared wavelengths," *Remote Sensing*, vol. 1, pp. 697–730, 2009.

[4] S. Salama, J. Monbaliu, and P. Coppin, "Atmospheric correction of advanced very high resolution radiometer imagery," *Int. J. Remote Sens.*, vol. 25, no. 7-8, pp. 1349–1355, 2004.

[5] G.A. Maul and H.R. Gordon, "On the use of the earth resources technology satellite (landsat-1) in optical oceanography," *Remote Sens. Environ.*, vol. 4, no. 0, pp. 95 – 128, 1975.

[6] A. Albert and C. Mobley, "An analytical model for subsurface irradiance and remote sensing reflectance in deep and shallow case-2 waters," *Opt. Express.*, pp. 2873–2890, 2003.

[7] H. Hakvoort, J. de Haan, R. Jordans, R. Vos, S. Peters, and M. Rijkeboer, "Towards airborne remote sensing of water quality in the netherlands – validation and error analysis," *ISPRS Journal of Photogrammetry and Remote Sensing*, vol. 57, no. 3, pp. 171–183, 2002.

[8] H. Schiller and R. Doerffer, "Improved determination of coastal water constituent concentrations from meris data," *IEEE Trans. Geosci. Remote Sens.*, vol. 43, no. 7, pp. 1585 – 1591, 2005.

[9] H.J. Van Der Woerd and R. Pasterkamp, "Hydropt: A fast and flexible method to retrieve chlorophyll-a from multispectral satellite observations of optically complex coastal waters," *Remote Sens. Environ.*, vol. 112, pp. 1795–1807, 2008.

[10] J.-P. Combe, P. Launeau, V. Carrère, Despan D., Méléder V., Barillé, and Sotin C., "Mapping microphytobenthos biomass by non-linear inversion of visible-infrared hyperspectral images," *Remote Sens. Environ.*, vol. 98, no. 4, pp. 371 – 387, 2005.

[11] N. Keshava and J.F. Mustard, "Spectral unmixing," *IEEE Sig. Proc. Mag.*, vol. 19, pp. 44–57, 2002.

[12] E. Knaeps, D. Raymaekers, S. Sterckx, L. Bertels, and D. Odermatt, "Monitoring inland waters with the apex sensor, a wavelet approach," in *Workshop on Hyperspectral Image and Sig. Proc.: Evolution in Remote Sensing (WHISPERS)*. 2010, pp. 1–4, IEEE.

[13] A.G. Dekker, *Detection of optical water quality parameters for eutrophic waters by high resolution remote sensing*, Vrije Universiteit Amsterdam, 1993.

[14] H. R. Gordon, O. B. Brown, R. H. Evans, J. W. Brown, R. C. Smith, K. S. Baker, and D. K. Clark, "A semianalytic radiance model of ocean color," *Journal of Geophysical Research: Atmospheres*, vol. 93, no. D9, pp. 10909–10924, 1988.

[15] IOCCG, *Remote Sensing of Inherent Optical Properties: Fundamentals, Tests of Algorithms, and Applications*, vol. No. 5 of *Reports of the International Ocean Colour Coordinating Group*, IOCCG, Dartmouth, Canada, 2006.

[16] M. Babin, D. Stramski, G. M. Ferrari, H. Claustre, A. Bricaud, G. Obolensky, and N. Hoepffner, "Variations in the light absorption coefficients of phytoplankton, nonalgal particles, and dissolved organic matter in coastal waters around europe," *Journal of Geophysical Research: Oceans*, vol. 108, no. C7, pp. 3211, 2003.

[17] B. Nechad, K.G. Ruddick, and Y. Park, "Calibration and validation of a generic multisensor algorithm for mapping of total suspended matter in turbid waters," *Remote Sens. Environ.*, vol. 114, no. 4, pp. 854–866, 2010.

[18] J. T. O. Kirk, *Light and Photosynthesis in Aquatic Ecosystems, 2nd ed.*, Cambridge University Press, New York, 1976.

[19] D. Auring and H. Dierssen, "Advantages and limitations of ocean color remote sensing in cdom-dominated, mineral-rich coastal and estuarine waters," *Remote Sens. Environ.*, vol. 125, no. 0, pp. 181–197, 2012.

[20] C.L. Lawson and R.J. Hanson, *Solving Least Squares Problems*, Prentice Hall, Englewood Cliffs, NJ, 1974.

[21] P. Kempeneers, S. Sterckx, W. Debruyn, S. DeBacker, P. Scheunders, P. Youngje, and K. Ruddick, "Retrieval of oceanic constituents from ocean color using simulated annealing," in *Proc. IEEE Int. Conf. Geosci. Remote Sens.*, 2005, vol. 8, pp. 5651–5654.

[22] S. Ufermann and University of Southampton, *Evaluation of a Semi-analytical Approach to the Retrieval of Water Quality Parameters from Optical Data in European Case-II Waters*, University of Southampton, 2003.

[23] J. Gutierrez, R. Rosario, and D. Sevilla, "On multivariate rational function decomposition," *J. Symb. Comput.*, vol. 33, no. 5, pp. 545–562, 2002.

[24] J.M. Bioucas-Dias, A. Plaza, N. Dobigeon, M. Parente, Qian Du, P. Gader, and J. Chanussot, "Hyperspectral unmixing overview: Geometrical, statistical, and sparse regression-based approaches," *IEEE J. Sel. Topics Appl. Earth Observ.*, vol. 5, no. 2, pp. 354–379, april 2012.

[25] N. Dobigeon, J.-Y. Tourneret, C. Richard, J.C.M. Bermudez, S. McLaughlin, and A.O. Hero, "Nonlinear unmixing of hyperspectral images: Models and algorithms," *IEEE Signal Process. Mag.*, vol. 31, no. 1, pp. 82–94, Jan 2014.

[26] R. Heylen, M. Parente, and P. Gader, "A review of nonlinear hyperspectral unmixing methods," 2014.

[27] D.C. Heinz and C.-I Chang, "Fully constrained least squares linear spectral mixture analysis method for material quantification in hyperspectral imagery," *IEEE Trans. Geosci. Remote Sens.*, vol. 39, no. 3, pp. 529–545, 2001.

[28] I-H. Lin, *Geometric linear algebra*, vol. 2, World Scientific, 2008.

[29] P. Bajorski, "Simplex projection methods for selection of endmembers in hyperspectral imagery," *Proc. IEEE Int. Conf. Geosci. Remote Sens.*, vol. 5, pp. 3207–3210, 2004.

[30] R. Heylen, D. Burazerovic, and P. Scheunders, "Fully constrained least squares spectral unmixing by simplex projection," *IEEE Trans. Geosci. Remote Sens.*, vol. 49, no. 11, pp. 4112–4122, 2011.

[31] M.D. Iordache, J. Bioucas-Dias, and A. Plaza, "Sparse unmixng of hyperspectral data," *IEEE Trans. Geosci. Remote Sens.*, vol. 6, no. 6, pp. 2014–2039, june 2011.

[32] M.D. Iordache, J.M. Bioucas-Dias, and A. Plaza, "Collaborative sparse regression for hyperspectral unmixing," *IEEE Trans. Geosci. Remote Sens.*, vol. 52, no. 1, pp. 341–354, 2014.

[33] R.M. Pope and E.S Fry, "Absorption spectrum (380 700 nm) of pure water: Ii. integrating cavity measurements," *Appl. Optics*, vol. 36, no. 33, pp. 8710–8723, 1997.

[34] K. G. Ruddick, V. De-Cauwer, and Y. J. Park, "Seaborne measurements of near infrared water-leaving reflectance: The similarity spectrum for turbid waters," *Armerican Society of Limnolgy and oceanography, Inc.*, vol. 51, no. 2, pp. 1167–1179, 2006.

[35] I. Dópido, A. Villa, and A. Plaza, "Unsupervised clustering and spectral unmixing for feature extraction prior to supervised classification of hyperspectral images," 2011.

[36] T. Glenn, D. Dranishnikov, P. Gader, and A. Zare, "Subpixel target detection in hyperspectral imagery using piece-wise convex spatial-spectral unmixing, possibilistic and fuzzy clustering, and co-registered lidar," in *Proc. IEEE Int. Conf. Geosci. Remote Sens.*, July 2013, pp. 1063–1066.

[37] A. K. Jain, M. N. Murty, and P. J. Flynn, "Data clustering: a review," *ACM Comput. Surv.*, vol. 31, no. 3, pp. 264–323, 1999.

[38] E.M. Ampe, E.L. Hestir, M. Bresciani, E. Salvadore, V.E. Brando, A. Dekker, T.J. Malthus, M. Jansen, L. Triest, and O. Batelaan, "A wavelet approach for estimating chlorophyll-a from inland waters with reflectance spectroscopy," *IEEE Geosci. Remote Sensing Lett.*, vol. 11, no. 1, pp. 89–93, 2014.

[39] N. Bolshakova and F. Azuaje, "Cluster validation techniques for genome expression data," *Signal Processing*, vol. 83, pp. 825–833, 2002.

[40] E.M. Winter, "N-FINDR: An algorithm for fast autonomous spectral end-member determination in hyperspectral data," *Proc. SPIE*, vol. 3753, pp. 266–275, 1999.

[41] Jos M. P. Nascimento and Jos M. B. Dias, "Vertex component analysis: a fast algorithm to unmix hyperspectral data.," *IEEE Trans. Geosci. Remote Sens.*, vol. 43, no. 4, pp. 898–910, 2005.

[42] K. Itten, F. DellEndice, A. Hueni, M. Kneubhler, D. Schlpfer, D. Odermatt, F. Seidel, S. Huber, J. Schopfer, T. Kellenberger, Y. Bhler, P. DOdorico, J. Nieke, E. Alberti, and K. Meuleman, "Apex - the hyperspectral esa airborne prism experiment," *Sensors*, vol. 8, pp. 6235–6259, 2008.

[43] P. Gege, J. Fries, P. Haschberger, P. Schoetz, H. Schwarzer, P. Strobl, B. Suhr, G. Ulbrich, and W. Jan Vreeling, "Calibration facility for airborne imaging spectrometers," *Journal of Photogrammetry and Remote Sensing*, vol. 64, pp. 387–397, 2009.

[44] J.F. De Haan and J.M.M. Kokke, "Remote sensing algorithm development toolkit: 1. operationalization of atmospheric correction methods for tidal and inland waters," *BCRS Report, RWS-Survey Department, Netherlands*, p. 91, 1996.

[45] S. Sterckx, E. Knaeps, and K. Ruddick, "Detection and correction of adjacency effects in hyperspectral airborne data of coastal and inland waters: the use of the near infrared similarity spectrum," *International Journal of Remote Sensing*, vol. ahead-of-p, pp. 1–27, 2011.

[46] S. Tassan and G.M. Ferrari, "An alternative approach to absorption measurements of aquatic particles retained on filters," *Limnology and Oceanography*, vol. 40, no. 8, pp. 1358–1368, 1995.

[47] G. Tilstone, G. Moore, K. Sorensen, R. Doerffer, R. Rottgers, K.G. Ruddick, R. Pasterkamp, and P.V. Jorgensen, "Regional validation of MERIS chl products in North Sea coastal waters: Protocols for the validation of MERIS products in case-2 waters," in *Proc. ENVISAT validation workshop*. October 2003, European Space Agency publications.

[48] E. Knaeps, A.I. Dogliotti, D. Raymaekers, K. Ruddick, and S. Sterckx, "In situ evidence of non-zero reflectance in the olci 1020nm band for a turbid estuary," *Remote Sens. Environ.*, vol. 120, no. 0, pp. 133 – 144, 2012.